Multifunctional Histidine Crosslinked Interface towards Efficient Planar Perovskite Solar Cells

Journal:	*ACS Applied Materials & Interfaces*
Manuscript ID	am-2022-13585p.R1
Manuscript Type:	Article
Date Submitted by the Author:	17-Sep-2022
Complete List of Authors:	Li, Yan; Beijing University of Chemical Technology Li, Siqi; Beijing University of Chemical Technology Shen, Yujie; Queen's University Belfast Han, Xue; Virginia Polytechnic Institute and State University, Chemical engineering Li, Yao; Beijing University of Chemical Technology Yu, Yingchun; Beijing University of Chemical Technology Huang, Meilan; Queen's University Belfast, School of Chemistry and Chemical Engineering Tao, Xia; Beijing University of Chemical Technology,

Multifunctional Histidine Crosslinked Interface towards Efficient Planar Perovskite Solar Cells

Yan Li[a], Siqi Li[a], Yujie Shen[b], Xue Han[c], Yao Li[a], Yingchun Yu[a], Meilan Huang[b], Xia Tao[a]**

a. State Key Laboratory of Organic-Inorganic Composites, Beijing University of Chemical Technology, Beijing 100029, China. E-mail: taoxia@mail.buct.edu.cn

b. School of Chemistry & Chemical Engineering, Queen's University Belfast, Belfast BT9 5AG, UK. E-mail: m.huang@qub.ac.uk

c. Department of Chemical Engineering, Virginia Polytechnic Institute and State University, Virginia 24061, United States

ABSTRACT: Interface engineering mediated by a designed chemical agent is of paramount importance for developing high-performance perovskite solar cells (PSCs). It is especially critical for planar SnO_2-based PSCs due to the presence of abundant surface defects on SnO_2 and/or perovskite surfaces. Herein, a novel multifunctional agent histidine (abbreviated as His) capable of crosslinking SnO_2 and perovskite is employed to modify the SnO_2/perovskite interface. Density functional theory (DFT) calculations and experimental results demonstrate that the carboxylate oxygen of His can form a Sn–O bond to fill the oxygen vacancies on the surface of SnO_2, while its positively charged imidazole ring can occupy the cationic vacancies and $–NH_3^+$ group interacts with the I^- ion on the perovskite lattice. This crosslinking contributes to the significantly decreased

interfacial trap state density and nonradiative recombination loss. In addition, it facilitates electron extraction/transfer and also improves interfacial contact and the quality of perovskite film. Correspondingly, His-modified device delivers a splendid champion power conversion efficiency (PCE) of 22.91% (improved from 20.13%) and an excellent open-circuit voltage (V_{oc}) of 1.17 V (improved from 1.11 V), along with significantly suppressed hysteresis. Furthermore, the unencapsulated device based on His modification shows much better humidity and thermal stability than the pristine one. The present work provides a guidance for the design of innovative multifunctional interfacial material for highly efficient PSCs.

KEYWORDS: *perovskite solar cells, defect passivation, histidine, interfacial modification, density functional theory calculations*

INTRODUCTION

Organic-inorganic hybrid perovskite solar cells (PSCs) have attracted amazing attention owing to the low-cost solution-processed method and high efficiency.[1,2] In the past few years, rapid advances in perovskite material itself and device stack via perovskite film quality optimization,[3-9] dimensionality engineering,[10-13] and interface engineering[14-18] have resulted in unprecedented advances; the power conversion efficiency (PCE) has been enhanced from initial 3.8%[19] to the certified 25.7%,[20] demonstrating the great commercialization potential of PSCs.

Electron transport layer (ETL) is a critical component of PSCs to promote the overall charge extraction efficiency. It serves as the basis for subsequent perovskite nucleation/crystallization and

protects the perovskite layer from moisture invasion in air simultaneously.[21-24] Therefore, ETL development has become one of major challenges to obtain high-performance PSCs. Recently, the low-temperature-processed and high-chemical-stability SnO_2 has been investigated broadly and demonstrated to be a highly promising ETL material in planar PSCs because of its high electron mobility (up to 240 $cm^2\ V^{-1}\ s^{-1}$), wide bandgap (3.6-4.0 eV), and favorable band alignment with the perovskite light-harvesting layer.[25-28] However, there still exist a large quantity of oxygen vacancies (V_O) and absorbed hydroxyl groups (–OH) on the surface of the solution-processed SnO_2 film.[27,29-32] Moreover, a great variety of unfavorable defects (under-coordinated Pb^{2+},[33-36] organic cation vacancies,[37] and halide vacancies,[38-40] etc.) will unavoidably generate in polycrystalline perovskite film during annealing and crystallization process.[41] These defects from the SnO_2 surface and the perovskite film bottom could act as the recombination centers at the SnO_2/perovskite interface, causing severe nonradiative recombination loss and decreased electron extraction rate,[42] and eventually resulting in an inferior open-circuit voltage (V_{oc}) and poor fill factor (FF).

Interface modification through introducing functional organic small molecule materials has been demonstrated to be a feasible and effective approach to optimize the electronic property of SnO_2 and improve SnO_2/perovskite interface state.[31,43-45] In recent years, organic small molecules with specific functional groups, such as carboxyl,[46] imidazole ring,[47,48] amino,[49,50] etc. have been extensively confirmed to passivate defects at perovskite surfaces and grain boundaries (GBs). For example, Zhou et al. employed an imidazole sulfonate zwitterion (IMS), which reacts using its

imidazolium moiety with the I^- ion of $MAPbI_3$ so as to obviously decrease trap state density, yielding an excellent PCE of 20.84%.[51] Yang et al. discovered a multiple functional passivator D-4-tert-butylphenylalanine (D4TBP) to comprehensively passivate perovskite defects, where the amine groups of D4TBP was suggested to alleviate the cation vacancy defects via electrostatic interactions, achieving an extremely small V_{oc} loss of 0.34 eV.[52] Apart from the aforementioned imidazolium moiety in IMS and the amine group in D4TBP, carboxyl group has shown effective in passivating GBs by crosslinking with Pb^{2+} ions of perovskite lattice.[53] What's more, carboxyl groups can also serve as a SnO_2 surface passivator via reacting with the –OH to form ester bond.[47] Inspired by these successful cases, we envisage that it would be possible to design and develop an all-in-one organic modifier containing various functional groups to resolve the puzzle behind the SnO_2/perovskite interface problem, that is, the simultaneously achieving passivating defects from the SnO_2 surface and the bottom of perovskite film, modulating perovskite layer crystallization and growth to passivate GBs, and achieving matched SnO_2/perovskite interfacial energy level beneficial for electron transport, etc.

In the present work, we develop a practical interfacial modification strategy where multifunctional histidine (His, containing carboxyl, imidazole ring and amino, etc. chemical structure is shown in Figure 1a) is introduced into SnO_2/perovskite, resulting in the simultaneous implementation of passivating interfacial defects, facilitating electron extraction/transfer, adjusting perovskite crystal growth and aligning SnO_2/perovskite interfacial energy level. Combining density functional theory (DFT) calculations and X-ray photoelectron spectroscopy

(XPS) results, we conclude that the carboxylate oxygen of His can form a Sn–O bond with the uncoordinated Sn, and fill the V_O defects on the surface of SnO_2, while the positively charged imidazole ring of His may occupy the cationic vacancies and $–NH_3^+$ may interact with the I^- ion of perovskite lattice. As a result, interfacial defect density is decreased and perovskite film quality is improved. Meanwhile, His molecules play a bridging role via forming coordination bonds or electrostatic interactions with the adjacent SnO_2 and perovskite layer, thereby improving interfacial adhesion and accelerating electron transfer from the perovskite to SnO_2 layer. Finally, the fabricated device based on His modification achieves an outstanding PCE up to 22.91% with increased V_{oc} (1.17 V) and FF (80.90%) as compared to the control PSC that provides a PCE of 20.13%, V_{oc} of 1.11 V, and FF of 77.02%, respectively. Furthermore, the unencapsulated His-treated device maintains 73.3% of the original PCE after aging for 1000 h under 20-40% RH in ambient conditions, whereas only 50.1% for the control device. This work presents an effective and practical approach for the SnO_2/perovskite interface modification to enhance the PSC performance.

RESULTS AND DISCUSSION

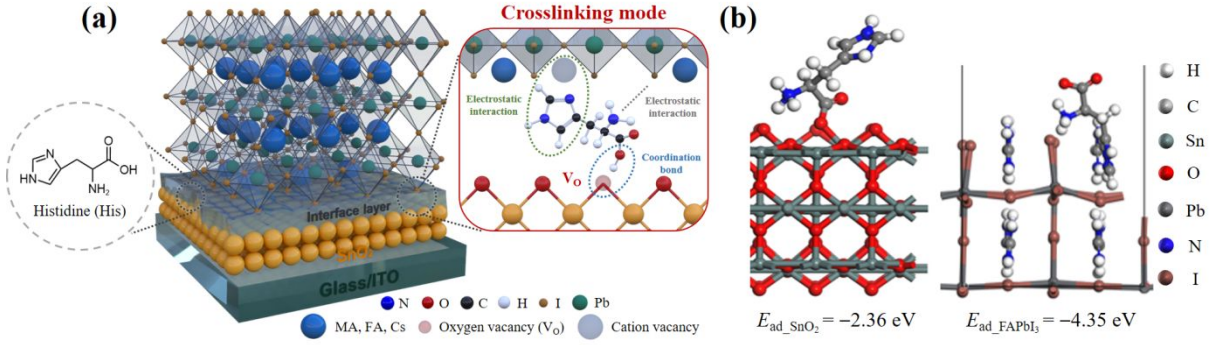

Figure 1. (a) Schematic illustration of the formation of His molecules between SnO_2 layer and perovskite layer. (b) Adsorption of His on the most stable termination of SnO_2 (110) surface in the presence of V_O with carboxylate ion pointing towards SnO_2 surface and on the optimized structure of $FAPbI_3$ (001) slab with FA vacancy.

Figure 1a depicts the modification mechanism of His interfacial layer between SnO_2 and perovskite layer. DFT calculations were adopted to elucidate the function of His at the SnO_2/perovskite interface (Figure 1b). According to the calculation results, when the carboxylate of His points towards the SnO_2 surface, the adsorption energy of His on the SnO_2 ($E_{ad\_SnO_2}$) and $FAPbI_3$ ($E_{ad\_FAPbI_3}$) surface are –2.36 eV and –4.35 eV, respectively, indicating strong interaction between His and SnO_2/perovskite layer. In this situation, the carboxylate oxygen of His forms a coordinate bond with Sn, (with a Sn–O bond distance of 2.21 Å) and fills the V_O; simultaneously the positively charged imidazole ring of His occupies the FA vacancy and its $–NH_3^+$ group interacts with the I^- ion on the perovskite lattice via electrostatic interaction. The total adsorption energy of His at the SnO_2/perovskite interface can be calculated based on the equation: $E_{ad} = E_{ad\_FAPbI_3} + E_{ad\_SnO_2}$ and the corresponding E_{ad} is –6.71 eV, demonstrating that His modification

results in strong crosslinking between SnO_2 and perovskite. To summarize, the strong adsorption energy of His at SnO_2/perovskite interface not only facilitates the passivation of interfacial defects and thus reduces the interfacial non-radiative recombination, but also improves the interface contact and the electron transport rate from perovskite to SnO_2 by bridging the SnO_2 and perovskite layers.

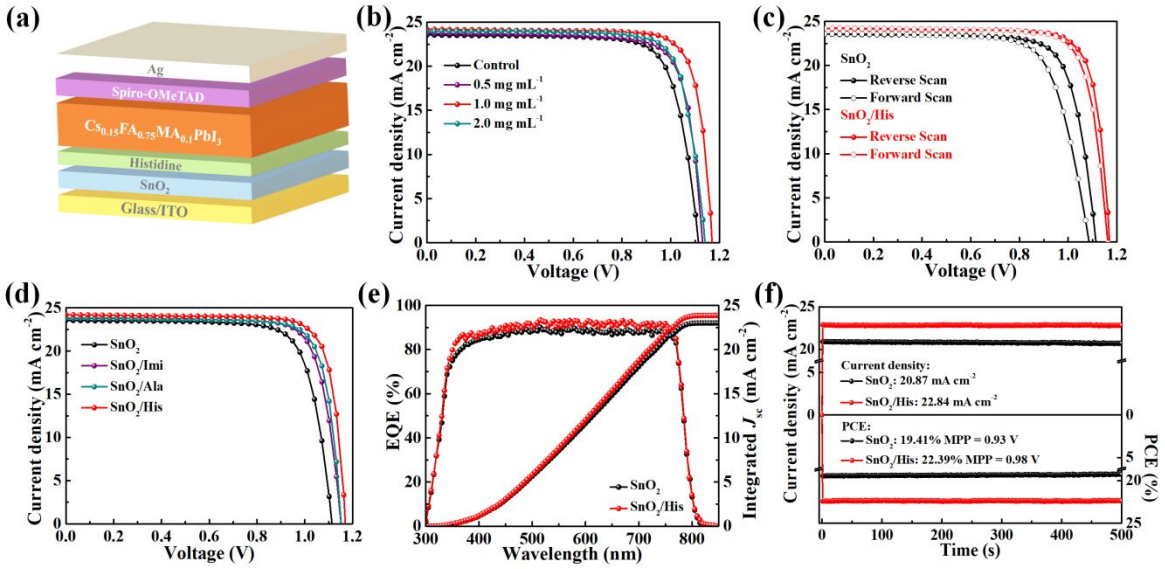

Figure 2. (a) Schematic architecture of the PSC. (b) *J-V* characters of PSCs based on SnO_2 and SnO_2/His ETLs with different concentrations from 0.5 to 2 mg mL^{-1}. (c) *J-V* characters of PSCs based on SnO_2 and SnO_2/His ETLs under reverse scan and forward scan. (d) *J-V* characters of PSCs based on SnO_2 and SnO_2/Imi or Ala or His ETLs. (e) EQE spectra and integrated J_{sc} curves and (f) steady-state power output at MPP of PSCs based on SnO_2 and SnO_2/His ETLs.

To investigate the effect of His-modified ETL on device performance, we fabricated PSCs with the structure of ITO/SnO_2/His/$Cs_{0.15}FA_{0.75}MA_{0.1}PbI_3$/Spiro-OMeTAD/Ag (Figure 2a). The

diluted commercial SnO_2 colloidal precursor (2.67 wt%) was spin-coated on the ITO substrate followed by annealing at 150 °C for 30 min. Subsequently, different concentrations of His aqueous solutions were spin-coated onto the formed SnO_2 film to fabricate the SnO_2/His layers (see the EXPERIMENTAL SECTION and Figure S1). It's worth noting that the His hardly undergoes dissolution in the solvent (DMSO) of perovskite precursors. Figure 2b displays the *J-V* characteristic curves for the champion PSC based on the SnO_2 and SnO_2/His ETLs with different concentrations from 0.5 to 2 mg mL^{-1}. The detailed photovoltaic parameters including PCE, V_{oc}, short-circuit current density (J_{sc}), and FF are presented in Table S1. The PSC based on pristine SnO_2 displays an inferior PCE of 20.13% along with a low V_{oc} (1.11 V), J_{sc} (23.55 mA cm^{-2}), and FF (77.02%). The addition of 0.5 mg mL^{-1} of His dramatically enhances the performance of PSC, achieving a PCE of 21.11% and V_{oc}, J_{sc}, and FF of 1.13 V, 23.76 mA cm^{-2}, and 78.76%, respectively. When the concentration of His increasing to 1 mg mL^{-1}, the PSC yields the champion PCE of 22.91% together with a V_{oc} of 1.17 V, J_{sc} of 24.21 mA cm^{-2}, and FF of 80.90% (Table S2). However, a higher concentration (2 mg mL^{-1}) of His leads to a decrease of efficiency ultimately, probably attributed to the accumulation of His at the SnO_2/perovskite and thus inhomogeneous perovskite films. Unless stated otherwise, subsequent characterization assays of His-treated samples are all based on 1 mg mL^{-1}. Furthermore, the PCE, V_{oc}, J_{sc}, and FF distributions of 20 cells without/with His modification are counted (Figure S2). His-treated PSCs show much narrower distribution and higher performance than the control PSCs, indicating high reproducibility of His-based PSCs. In addition, *J-V* curves based on the two ETLs under both forward- and reverse-scan

directions were measured and recorded (Figure 2c and Table S3). Obviously, the hysteresis is largely suppressed with the His treatment. The hysteresis index of His-based PSC is decreased to 0.024 from 0.079 for the control PSC, implying the improved charge transport process due to the His modification.

Considering the multifunctional properties of His in combination with imidazole ring, amine, and carboxyl functional groups, we herein propose that the individual moiety of His may play a positive role in enhancing the device performance. We therefore divided His molecule into two neutral segments i.e., imidazole (Imi) and alanine (Ala), respectively. Specifically, Imi or Ala with the same concentration of His was added onto SnO_2 layer and then implemented the fabrication of different control devices. Ultimately, we found that the PCEs of 21.64% and 22.01% were achieved from the Imi and Ala-treated devices respectively, but both are still lower than that of the His-modified device (22.91%) (Figure 2d and Table S4). The higher performance of His-modified device may be attributed to the multiple functional groups of His, which are able to synergistically passivate more defects.

The light response of device was investigated by external quantum efficiency (EQE) spectra (Figure 2e). The integrated current density for the PSC before and after His treatment are 23.01 and 23.86 mA cm^{-2}, respectively, which matches well with the *J-V* curve results. Subsequently, steady-state power output at maximum power point (MPP) was measured (Figure 2f). It shows that the stabilized PCEs of 19.41% and 22.39% are achieved after illumination under 1 sun for 500 s from the control and His-modified perovskite devices, respectively.

XPS measurement was conducted to investigate the chemical interaction between SnO_2 and His for in-depth understanding the mechanism of device performance enhancement. The XPS full spectra of bare SnO_2 and SnO_2/His films are depicted in Figure 3a. Compared with bare SnO_2 film, the occurrence of N 1s (Figure 3b) in SnO_2/His film demonstrates the successful binding of His to the SnO_2 surface. In addition, a strong chemical interaction is formed between His and Sn as demonstrated by the shift of the Sn $3d_{3/2}$ and Sn $3d_{5/2}$ peaks, which move (from 494.8 eV and 486.3 eV in the pristine SnO_2) to higher binding energy (495.1 and 486.7 eV for the His-modified SnO_2, respectively) (Figure 3c). Furthermore, it is observed that O 1s spectra for the two samples is split into two peaks (Figure 3d,e) i.e., a high binding energy peak corresponding to oxygen vacancies (V_O) on the SnO_2 surface and a low binding energy peak associated with the saturated oxygen (O^{2-}). The shift (from 530.2 to 530.6 eV) of the O^{2-} peak further manifests the interaction between SnO_2 and His.[50] In addition, the peak areas of V_O and O^{2-} can well reflect the contents of V_O and O^{2-}, respectively. The calculated proportion of V_O in His-treated SnO_2 is decreased to 0.33 from 0.42 in pristine SnO_2, indicating that V_O is effectively passivated via the Sn–O coordinate bond formed by the interaction of the carboxylate oxygen in His and the Sn in SnO_2. The passivated V_O can decrease the probability of electrons captured by the defects at the SnO_2 surface and thus contribute to electron transport at the SnO_2/perovskite interface.

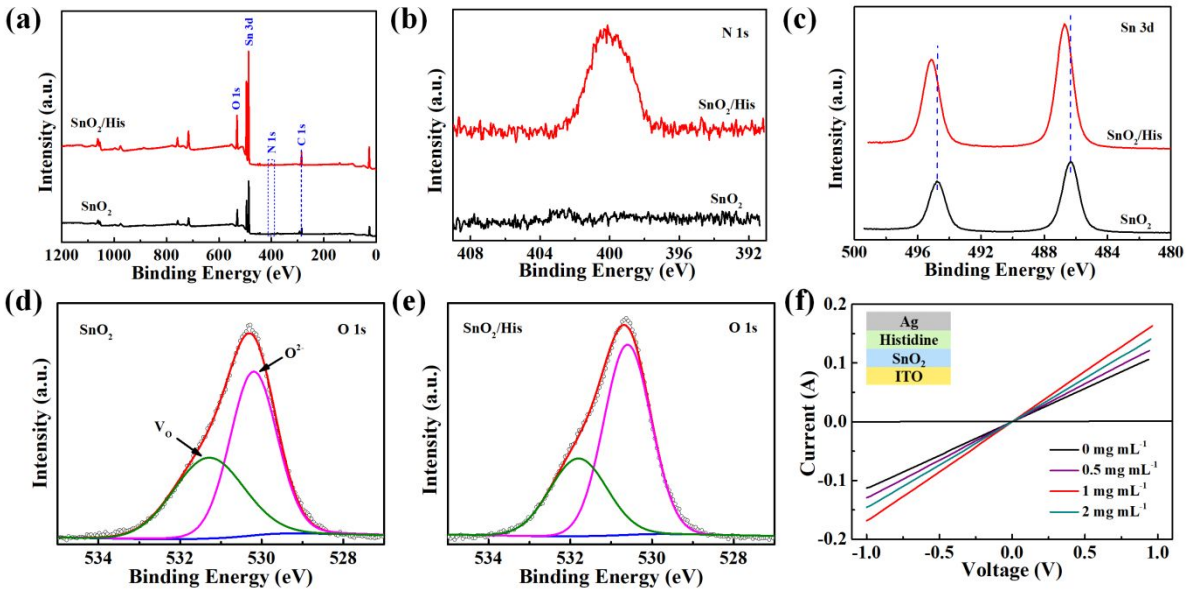

Figure 3. (a) XPS full spectra of SnO_2 and SnO_2/His films. XPS high-resolution spectra of SnO_2 and SnO_2/His films for (b) N 1s, (c) Sn 3d and (d), (e) O 1 s. (f) *I-V* curves of devices based on SnO_2 and SnO_2/His ETLs with different concentrations from 0.5 to 2 mg mL^{-1}. The inset depicts the device structure.

It's worth mentioning that the roughness and wettability of ETL substrate is the key to the crystallization and growth of upper perovskite layer,[44] and hence the PSC performance. According to the atomic force microscopy (AFM) results (Figure S3), the surface root mean square (RMS) roughness is 3.55 and 2.92 nm for pristine and His-modified SnO_2, respectively. Thus much more homogeneous and smoother surface morphology in SnO_2/His film can promote the formation of high-quality perovskite films. Subsequently, we further measured the contact angle by dropping perovskite precursor solution on SnO_2 films without/with His modification and found that the presence of additional His layer shows no significant influence on the overall surface wettability

and the perovskite solution could spread out completely in 5 s (Figure S4). Moreover, His has no significant effect on the crystallinity and optical transmittance of pristine SnO_2 film (Figure S5 and S6a).

The optical band gap of the pristine and His-treated SnO_2 were determined by corresponding Tauc plots derived from UV-vis absorption spectra (UV-vis), which show values of 4.03 and 4.02 eV, respectively (Figure S6b). To investigate the conductivity of SnO_2 films before and after His modification, devices with the structure of ITO/SnO_2/His/Ag were manufactured. On the basis of the *I-V* curves (Figure 3f) and the equation: $I = V\sigma A/d$ (A is the device area and d is the thickness of the ETL),[50,54,55] notably increased conductivity is observed in His-treated SnO_2 film (12.85×10^{-3} mS cm^{-1}, C_{His} = 1 mg mL^{-1}) in comparison with the pristine one (8.47×10^{-3} mS cm^{-1}). This is mainly attributed to the newly formed Sn–O bond and the passivated V_O that can effectively reduce interfacial charge accumulation.[46] However, a higher concentration of His will increase device's series resistance (R_s) and result in a decreased conductivity (11.09×10^{-3} mS cm^{-1}, C_{His} = 2 mg mL^{-1}), which is in line with the *J-V* characteristic curves results (Figure 2b).

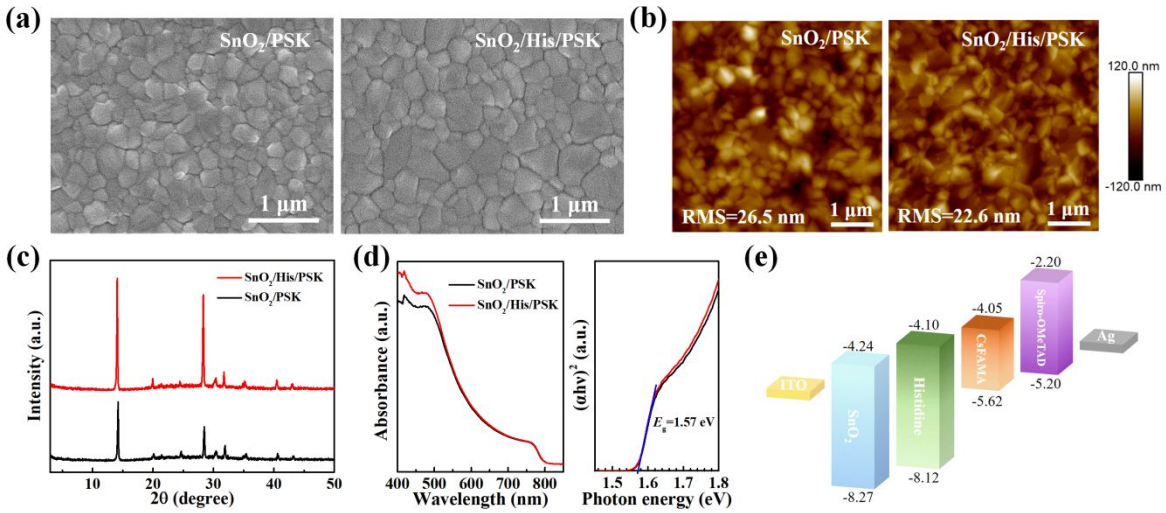

Figure 4. (a) SEM and (b) AFM images of perovskite films deposited on SnO_2 and SnO_2/His ETLs. (c) XRD patterns, (d) UV-vis and Tauc plots of perovskite films. (e) The energy level diagram of the PSC.

For in-depth understanding the influence of the interface modification on the morphology of upper perovskite layers, top-view and cross-sectional scanning electron microscopy (SEM) measurements were employed (Figure 4a and Figure S7). A uniform, full-coverage, and non-pinhole perovskite film is obtained but with distinctly different grain sizes. After His treatment, the average grain size of perovskite film increases from 360 nm to 480 nm (Figure S8). Subsequently, AFM measurement was conducted to investigate the surface roughness of the perovskite layers deposited on pristine and His-modified SnO_2 films. A lower RMS roughness of 22.6 nm is observed for the perovskite film deposited on His-treated SnO_2 (Figure 4b). In addition, X-ray diffraction (XRD) and UV-vis were adopted to separately explore the impact of different ETLs on crystallization and optical absorption of perovskite. A remarkably enhanced crystallinity

and a slightly strong optical absorption are observed for the perovskite film growing on the His-modified SnO_2 (Figure 4c,d). The above results demonstrate that His can promote the growth of perovskite layer and contribute to the formation of high-quality perovskite film with large grains and high crystallinity. This ultimately helps to protect the perovskite layer from moisture in the air and improves device stability. The band gap of perovskite is also calculated via UV-vis and corresponding Tauc plots, and a value of 1.57 eV is observed for the two perovskite films (Figure 4d). Since the band alignment of ETL and perovskite has a significant impact on the electron extraction/transfer at the ETL/perovskite, ultraviolet photoelectron spectroscopy (UPS) measurement was performed to investigate the changes in the conduction band (E_{CB}) position of SnO_2 without and with His modification. The E_{CB} values of pristine SnO_2, His-modified SnO_2, and perovskite films were identified as –4.24, –4.10, and –4.05 eV, respectively (Figure 4e and Figure S9). Thus it is apparent that the E_{CB} of His-treated SnO_2 is closer to that of perovskite, which is favorable for decreasing interface energy barrier, suppressing interface recombination and providing a more effective electron extraction.

Additionally, we conducted steady-state photoluminescence (SSPL) and time-resolved photoluminescence (TRPL) measurements to further confirm the passivation effect of His on the defects from the perovskite film bottom. As illustrated in Figure 5a, the SSPL intensity of the perovskite film deposited on His-coated glass is visibly higher than that on bare glass, demonstrating obviously reduced defects due to the His passivation. The TRPL decay curves (Figure 5b) are fitted with biexponential decay formula: $I(t) = I_0 + A_1\exp(-t/\tau_1) + A_2\exp(-t/\tau_2$

).[56] The carriers average lifetime can be determined via the equation: $\tau_{avg} = (A_1 * \tau_1 + A_2 * \tau_2)/A_1 + A_2$. The τ_{avg} of His-modified perovskite film (τ_{avg} = 493.45 ns, τ_1 = 1.55 ns, and τ_2 = 495.57 ns) is prolonged distinctly as compared to the pristine film (τ_{avg} = 280.25 ns, τ_1 = 2.92 ns, and τ_2 = 291.36 ns) (Table S5), demonstrating the clearly decreased nonradiative recombination. SSPL and TRPL analyses were also performed to explore the variations of charge extraction/transfer process at the SnO_2/perovskite without and with His treatment. Glass/SnO_2/His/PSK sample yields a stronger PL quenching (Figure 5c), indicating better electron extraction ability for the His-treated SnO_2 ETL. According to the TRPL spectra and corresponding fitting parameters (Figure 5d and Table S6), the Glass/SnO_2/His/PSK sample exhibits shorter decay time of 91.74 ns as compared to the Glass/SnO_2/PSK sample of 160.39 ns, suggesting stronger electron transport capacity at the SnO_2/His/PSK interface originating from the bridging function of His and also the favorable energy band alignment between the His-modified SnO_2 and perovskite.

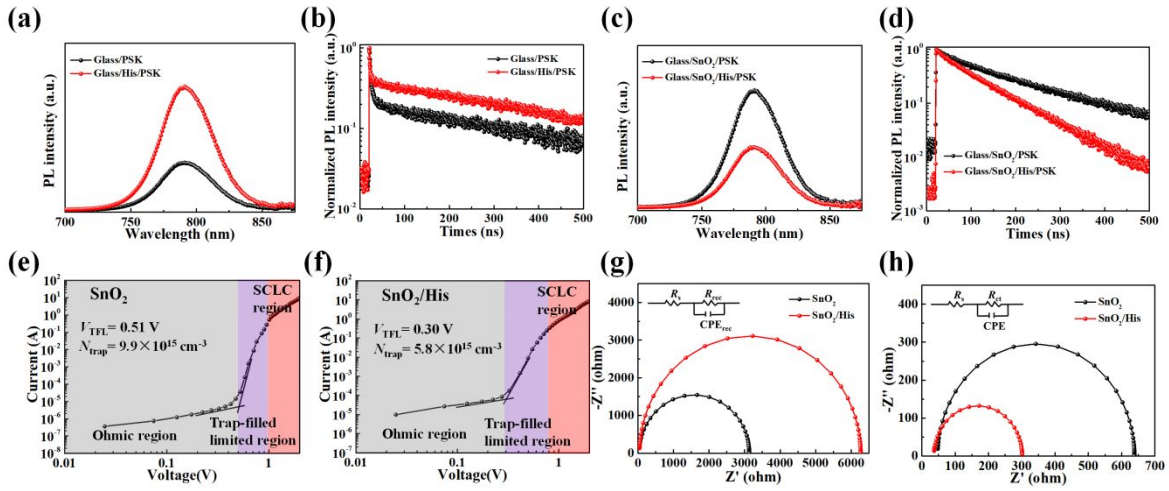

Figure 5. (a) SSPL spectra and (b) TRPL decays of perovskite films deposited on bare glass and on His, respectively. (c) SSPL spectra and (d) TRPL decays of perovskite films deposited on SnO_2

and SnO_2/His ETL, respectively. Dark *I-V* curves for the electron-only devices based on (e) pristine SnO_2 and (f) SnO_2/His ETLs. Nyquist plots of PSCs based on pristine SnO_2 and SnO_2/His ETLs, obtained on a bias voltage of 0.8 V under (g) dark condition and (h) 1 sun illumination. The corresponding equivalent circuits for fitting are shown in the inset, in which R_{rec} and R_{ct} represent recombination resistance and transfer resistance, respectively.

To evaluate the trap state density (N_{trap}) of devices without/with His modification, we fabricated electron-only devices with a structure of ITO/ETL/perovskite/PCBM/Ag based on the space charge-limited current (SCLC) model, with corresponding *J-V* curves displayed in Figure 5e,f. The N_{trap} is calculated via the trap-filled limit voltage (V_{TFL}) formula as follows: $N_{trap} = 2V_{TFL}\varepsilon\varepsilon_0/qL^2$, where L is the thickness of perovskite film, q is elementary charge, ε is the relative dielectric constant of perovskite, ε_0 is the vacuum permittivity, and V_{TFL} is the onset voltage of the trap-filled limit region, respectively. The calculated N_{trap} of devices without/with His treatment are 9.9×10^{15} and 5.8×10^{15} cm^{-3}, respectively. The decreased defect density is ascribed to the reduced interfacial charge recombination and improved perovskite film quality caused by His passivation. Electrochemical impedance spectroscopy (EIS) measurement was performed to further assess the interfacial charge transfer and recombination behavior. The Nyquist plots of the PSCs without/with His modification at a bias voltage of 0.8 V under dark condition and AM 1.5G are exhibited in Figure 5g,h. Larger R_{rec} and smaller R_{ct} are observed for the His-treated devices (Table S7 and S8), indicating effectively suppressed charge recombination, and improved electron

extraction after His loaded onto the SnO_2 layer.

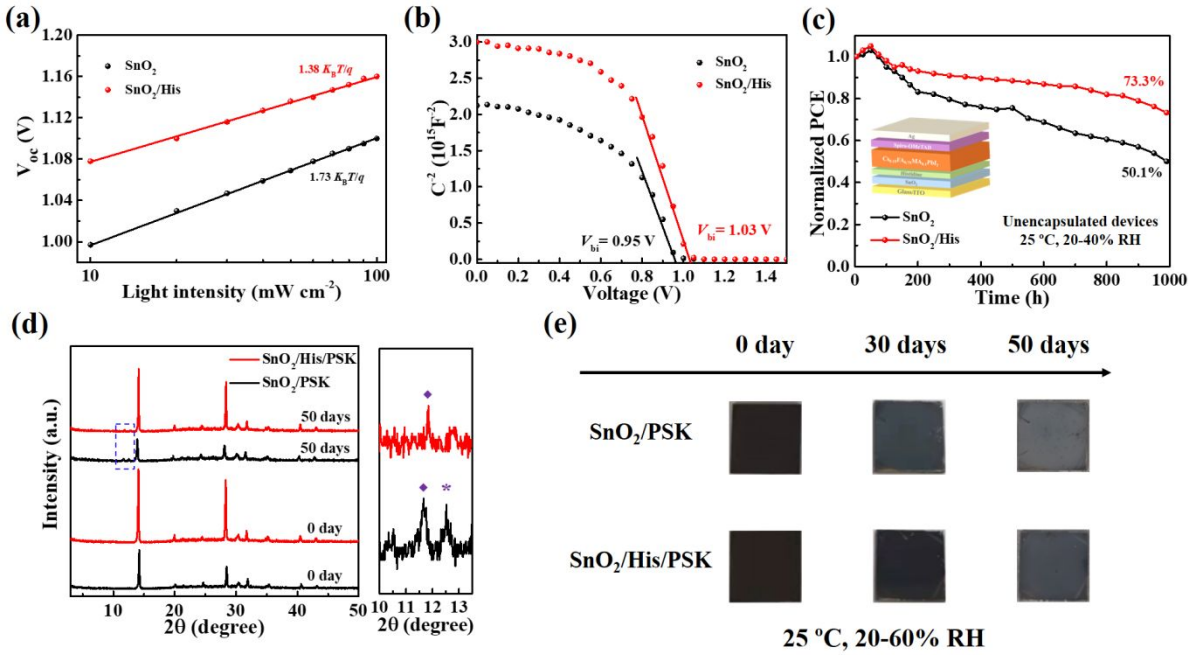

Figure 6. (a) V_{oc} versus light intensity and (b) Mott-Schottky analysis at 10 kHz of PSCs based on pristine SnO_2 and SnO_2/His ETLs. (c) PCE evolution of the unencapsulated devices based on pristine SnO_2 and SnO_2/His ETLs in ambient conditions (25 °C, 20-40% RH). (d) XRD patterns of perovskite films deposited on SnO_2 and SnO_2/His ETLs before and after ambient (20-60% RH) storage for 50 days, the " * " signal and the " ♦ " signal corresponding to the PbI_2 diffraction peak and the perovskite hydrated phase diffraction peak, respectively. (e) Photos of the perovskite films deposited on SnO_2 and SnO_2/His ETLs exposed to 20-60% RH ambient air for different days.

To gain further insight into the positive effect of the His modification on device performance, the carrier transport and recombination process of devices were systematically explored. *J-V* curves of devices under different light intensities (φ) were recorded, with the derived V_{oc} and J_{sc}

versus φ illustrated in Figure 6a and Figure S10a. The equation involved is displayed as follows: $V_{oc} = nK_BT\ln(\varphi)/q$, where T is the temperature, K_B is the Boltzmann constant, and n is the ideal factor, respectively. The n value is close to 1 when radiative recombination prevails. On the contrary, when the trap-assisted nonradiative recombination dominates, the n value is close to 2. The n value decreases from 1.73 to 1.38 after His treatment (Figure 6a), which implies depressed nonradiative recombination. The decreased nonradiative recombination may be attributed to the promoted charge transfer between perovskite and His-modified SnO_2 layer as well as the improved quality of perovskite film caused by His passivation. The α value of 0.991 for His-treated device is closer to 1 as compared to the control device ($\alpha = 0.975$) (Figure S10a), demonstrating a weaker bimolecular recombination.[48] The impact of ETL on the built-in potential (V_{bi}) of the devices without/with His treatment were investigated by Mott-Schottky analysis. The His-treated PSC shows V_{bi} (1.03 V) much higher than pristine SnO_2 based PSC (0.95 V) (Figure 6b). In addition, the His-modified perovskite device shows much lower dark current density than control device (Figure S10b), which indicates significantly decreased charge recombination and enhanced charge extraction. The above results also well illustrate that the improvement of V_{oc} (1.11 V → 1.17 V) is mainly ascribed to the dramatically reduced trap state density and enhanced driving force of photogenerated carrier separation with the passivation of His.

Considering the above characterizations and performance analysis, we propose that His regulates SnO_2/perovskite interface via two independent but synergistic effects. One effect is to act as a SnO_2 surface modifier by passivating the V_O defects and elevating the electron extraction

rate. The other effect is to neutralize the charged defects at the bottom surface of perovskite layer and modulate the crystallization and growth of perovskite layer. These multifunctional and synergistic effects of His in crosslinking SnO_2 and perovskite spontaneously occur during PSC fabrication without the need of complex process control.

The long-term stability of PSCs plays a crucial role in their further advancement and commercial applications.[57-63] The humidity stability of unencapsulated PSCs without/with His treatment were thus evaluated under 20-40% RH (Figure 6c). After aging for 1000 h, the PCE of control device declines to 50.1% of the initial value. However, the His-modified perovskite device retains 73.3% of its original PCE under the same condition, indicating a notably enhanced humidity stability. In addition, the moisture resistance capability of perovskite films without/with His treatment exposed to ambient air (20-60% RH) for 50 days was investigated by XRD (Figure 6d), and the photos of perovskite films aging for different days were recorded accordingly (Figure 6e). With the exposure time up to 50 days, many clearly visible pinholes/cracks are observed in pristine perovskite film. The structure variation in film may be attributed to the decomposition of perovskite layer, which is also demonstrated by the newly appeared PbI_2 peak (marked with " * ") (Figure 6d). On the contrary, it can be observed that His-modified film still maintains a no-pinhole surface and relative high crystallinity even after 50-day aging. The reasons for the excellent moisture stability of His-modified perovskite device are: i) the improved quality of perovskite film itself that is mainly owing to the enhanced film crystallinity, the reduction of defects and grain boundary numbers induced by His passivation, and ii) the improved interfacial contact and

adhesion caused by His-mediated crosslinking of the SnO_2 and perovskite layers that alleviates the moisture-induced perovskite decomposition. Thermal stability of the unencapsulated devices was measured at 60 °C in nitrogen-filled glove box. After aging for 300 h, the control device has only 71.6% of the initial PCE, while the His-modified device maintains 84.1% of its original PCE (Figure S11). Obviously, the thermal stability is also improved after interface modification.

CONCLUSIONS

In summary, we report an all-in-one multifunctional interface modifier His to modify SnO_2/perovskite interface to obtain high-performance planar PSCs. DFT calculations and experimental results demonstrate that the crosslinking of His between the SnO_2 and perovskite layer can not only effectively passivate the interfacial defects to reduce interfacial nonradiative recombination loss but also improve the interface contact to elevate the electron extraction rate and facilitate the growth of perovskite crystals. In addition, the His modification can realign the conduction band of SnO_2 upward to further accelerate interfacial electron transfer. As a result, the fabricated PSC based on His-modified SnO_2 produces an outstanding PCE of 22.91%, along with a V_{oc} of 1.17 V, J_{sc} of 24.21 mA cm^{-2}, and FF of 80.90%. Finally, due to passivated interfacial defects and improved quality of perovskite film, the His-based PSCs exhibit superior humidity and thermal stability. The unencapsulated His-treated device maintains 73.3% of the initial PCE after aging for 1000 h in ambient conditions (20-40% RH) and 84.1% of its original PCE after aging for 300 h at 60 °C, respectively. The present work provides a guidance for the design and

development of interface modification molecules containing multiple functional groups towards realizing highly efficient and stable planar PSCs.

EXPERIMENTAL SECTION

Materials. ITO glass substrates (15 Ω cm^{-2}) were purchased from ShenZhen South China Xiang Science & Technology Company Limited. CsI (99.999%) and SnO_2 colloidal dispersion (15% wt%) were purchased from Alfa Aesar. 2,2',7,7'-tetrakis-(*N*,*N*-di-*p*-methoxyphenylamino)-9,9'-spirobi-fuorene (Spiro-OMeTAD, > 99.8%), PbI_2 (> 99.99%), MACl, and 4-*tert*-butylpyridine (tBP, 96%) were purchased from Xi'an Polymer Light Technology Corp. MAI and FAI were purchased from Greatcell Solar Materials. acetonitrile (99.8%) and lithium bis(trifluoromethanesulfonyl)imide (Li-TFSI, 99.95%) were purchased from Sigma-Aldrich. Histidine (His, > 98%) was purchased from Sinopharm Chemical Reagent Co. LTD. Imidazole (Imi, > 99%) was purchased from TCI. Alanine (Ala, > 98.5%) was purchased from bidepharm. chlorobenzene (CB, 99.8%), isopropanol (IPA, 99.5%) and Dimethyl sulfoxide (DMSO, 99.9%) were purchased from J&K Chemical Ltd. All experimental agents were purchased and used directly without purification process.

Solar cells fabrication. ITO-patterned substrates were washed thoroughly with DI water, ethanol, and IPA, respectively, and subsequently processed with an UV-ozone surface cleaner for 20 min. The SnO_2 colloid dispersion was pre-diluted to 2.67 wt% with DI water and stirred overnight. The SnO_2 aqueous solution was spin-coated (3000 rpm, 30 s) on ITO substrates, and

annealed (150 °C, 30 min) in ambient air. His aqueous solution was prepared with different concentrations from 0.5 to 2 mg mL^{-1}. Subsequently, His or Imi or Ala surface modification layer was also spin-coated (3000 rpm, 30 s) on already formed ITO/SnO_2 film and annealed (100 °C, 10 min). Afterwards, all of samples were transferred into nitrogen-filled glovebox. For perovskite precursor, 553.2 mg PbI_2, 154.7 mg FAI, 46.8 mg CsI, 19.1 mg MAI, and 15.5 mg MACl were dissolved in 1 mL DMSO at 60 °C. Afterwards, the already formed precursor solution was spin-coated onto ITO/ETL substrates via a two-step (1000 rpm 10 s, 6000 rpm 30 s) process. At 6 s before the competition of the second step, 150 μL of CB was gently dropped on the substrate and then the perovskite precursor films were annealed (110 °C, 5 min). The Spiro-OMeTAD solution composed of 72.3 mg of Spiro-OMeTAD, 28.8 μL of tBP, 17.5 μL of Li-TFSI (520 mg Li-TFSI dissolved in 1 mL acetonitrile), and 1 mL of CB was spin-coated (2500 rpm, 30 s) onto the perovskite layer. At last, the 80 nm thick silver was thermally evaporated under high vacuum (< 5×10^{-4} Pa) as top electrode.

Characterization. Film and device characterizations are provided in Supporting Information.

Computational methods. All calculations in this work were carried out based on the DFT using Vienna ab Initio Simulation Package (VASP).[64] The cut-off energy was set at 400 eV. The perovskite structure is simplified as the $FAPbI_3$ that is the major component of the studied perovskite with mixed composition. A 3×3×3 Monkhorst-Pack k-point mesh sampling for Brillouin-zone was used to optimize the $FAPbI_3$ unit cell.[65] Because the cubic-$FAPbI_3$ structure has been detected from high resolution neutron powder diffraction data at 298 K, with the lattice

parameter 6.36 Å,[66,67] the cubic structure was used in our calculations. The optimized lattice of cubic-$FAPbI_3$ was 6.36 Å which agreed well with the literature data. The (001) facet has been proved to be the most stable surface in a cubic perovskite structure,[68] and hence the cubic-$FAPbI_3$ (001) surface was used in this work. For the SnO_2 structure, SnO_2 (110) is the most stable surface in the presence of V_O.[69] Both the $FAPbI_3$ (001) and SnO_2 (110) surfaces possess different terminations.[46,70] $FAPbI_3$ (001) with FA termination and SnO_2 (110) with the most stable T3 termination were used in our calculations.

The $FAPbI_3$ (001) surface was created by a 2×2 supercell with 15Å-thick vacuum layer to avoid interactions with the periodic slabs. A 2×2×1 k-point mesh was used to optimize all the structures. The SnO_2 (110) surface was created by a 2×1 supercell with 15Å-thick vacuum layer and the k-point point mesh was set at 3×3×1 to optimize all structures. The histidine with protonated imidazole generally shows stronger adsorption energy than the neutral one (Figure S12 and Table S9). Therefore, the protonated histidine is adopted in our calculations. Adsorptions of histidine molecule on the $FAPbI_3$ (001) slab with FA vacancy and the SnO_2 (110) surface in the presence of V_O were calculated. Finally, the adsorption energy of histidine on SnO_2 was calculated as $E_{ad\_SnO_2} = E_{SnO_2\_histidine} - E_{vacancy\_slab} - E_{histidine}$ and the adsorption energy of histidine on $FAPbI_3$ was calculated as $E_{ad\_FAPbI_3} = E_{FAPbI_3\_histidine} - E_{vacancy\_slab} - E_{histidine}$.

ASSOCIATED CONTENT

Supporting Information

Detailed characterizations of film and device, process flow chart, AFM images, contact angles, XRD patterns, cross-sectional SEM images, grain sizes, UPS spectra, detailed photovoltaic parameters, TRPL and EIS fitting parameters.

AUTHOR INFORMATION

Corresponding Authors

Meilan Huang – *School of Chemistry & Chemical Engineering, Queen's University Belfast, Belfast BT9 5AG, UK.* E-mail: m.huang@qub.ac.uk

Xia Tao – *State Key Laboratory of Organic-Inorganic Composites, Beijing University of Chemical Technology, Beijing 100029, China.* E-mail: taoxia@mail.buct.edu.cn

Authors

Yan Li – *State Key Laboratory of Organic-Inorganic Composites, Beijing University of Chemical Technology, 15 Beisanhuan East Road, Beijing 100029, China.*

Siqi Li – *State Key Laboratory of Organic-Inorganic Composites, Beijing University of Chemical Technology, 15 Beisanhuan East Road, Beijing 100029, China.*

Yujie Shen – *School of Chemistry & Chemical Engineering, Queen's University Belfast, Belfast BT9 5AG, UK.*

Xue Han – *Department of Chemical Engineering, Virginia Polytechnic Institute and State University, Virginia 24061, United States.*

Yao Li – *State Key Laboratory of Organic-Inorganic Composites, Beijing University of Chemical Technology, 15 Beisanhuan East Road, Beijing 100029, China.*

Yingchun Yu – *State Key Laboratory of Organic-Inorganic Composites, Beijing University of Chemical Technology, 15 Beisanhuan East Road, Beijing 100029, China.*

Notes

The authors declare no competing financial interest.

ACKNOWLEDGMENTS

This work was financially supported by the National Natural Science Foundation of China (No: 22176011) and the Opening Project of State Key Laboratory of Organic-Inorganic Composites.

REFERENCES

(1) Yin, W. J.; Shi, T.; Yan, Y. Unique Properties of Halide Perovskites as Possible Origins of the Superior Solar Cell Performance. *Adv. Mater.* **2014**, *26*, 4653-4658.

(2) Dunlap-Shohl, W. A.; Zhou, Y.; Padture, N. P.; Mitzi, D. B. Synthetic Approaches for Halide Perovskite Thin Films. *Chem. Rev.* **2019**, *119*, 3193-3295.

(3) Zhang, F.; Zhu, K. Additive Engineering for Efficient and Stable Perovskite Solar Cells. *Adv. Energy Mater.* **2020**, *10*, 1902579.

(4) Liang, L.; Luo, H.; Hu, J.; Li, H.; Gao, P. Efficient Perovskite Solar Cells by Reducing Interface -Mediated Recombination: a Bulky Amine Approach. *Adv. Energy Mater.* **2020**, *10*, 2000197.

(5) Song, S.; Park, E. Y.; Ma, B. S.; Kim, D. J.; Park, H. H.; Kim, Y. Y.; Shin, S. S.; Jeon, N. J.;

Kim, T. S.; Seo, J. Selective Defect Passivation and Topographical Control of 4 - Dimethylaminopyridine at Grain Boundary for Efficient and Stable Planar Perovskite Solar Cells. *Adv. Energy Mater.* **2021**, *11*, 2003382.

(6) Qiu, L.; Xing, K.; Zhang, J.; Yang, Y.; Cao, W.; Zhou, X.; Zhu, K.; Xia, D.; Fan, R. Two-Dimensional Metal-Organic Frameworks - Based Grain Termination Strategy Enables High - Efficiency Perovskite Photovoltaics with Enhanced Moisture and Thermal Stability. *Adv. Funct. Mater.* **2021**, *31*, 2010368.

(7) Liu, C.; Liu, S.; Wang, Y.; Chu, Y.; Yang, K.; Wang, X.; Gao, C.; Wang, Q.; Du, J.; Li, S.; Hu, Y.; Rong, Y.; Guo, L.; Mei, A.; Han, H. Improving the Performance of Perovskite Solar Cells via a Novel Additive of N,1-Fluoroformamidinium Iodide with Electron-Withdrawing Fluorine Group. *Adv. Funct. Mater.* **2021**, *31*, 2010603.

(8) Ma, D.; Li, W.; Chen, X.; Yang, Z.; Zhao, J.; Yang, Z.; Zhang, Y.; Chi, Z. An Effective Strategy of Combining Surface Passivation and Secondary Grain Growth for Highly Efficient and Stable Perovskite Solar Cells. *Small* **2021**, *17*, 2100678.

(9) Chen, L.; Wan, L.; Li, X.; Zhang, W.; Fu, S.; Wang, Y.; Li, S.; Wang, H.-Q.; Song, W.; Fang, J. Inverted All-Inorganic $CsPbI_2Br$ Perovskite Solar Cells with Promoted Efficiency and Stability by Nickel Incorporation. *Chem. Mater.* **2019**, *31*, 9032-9039.

(10) Lee, J. W.; Dai, Z.; Han, T. H.; Choi, C.; Chang, S. Y.; Lee, S. J.; De Marco, N.; Zhao, H.; Sun, P.; Huang, Y.; Yang, Y. 2D Perovskite Stabilized Phase-Pure Formamidinium Perovskite Solar Cells. *Nat. Commun.* **2018**, *9*, 3021.

(11) Gharibzadeh, S.; Abdollahi Nejand, B.; Jakoby, M.; Abzieher, T.; Hauschild, D.; Moghadamzadeh, S.; Schwenzer, J. A.; Brenner, P.; Schmager, R.; Haghighirad, A. A.; Weinhardt, L.; Lemmer, U.; Richards, B. S.; Howard, I. A.; Paetzold, U. W. Record Open-Circuit Voltage Wide-Bandgap Perovskite Solar Cells Utilizing 2D/3D Perovskite Heterostructure. *Adv. Energy Mater.* **2019**, *9*, 1803699.

(12) Mahmud, M. A.; Duong, T.; Yin, Y.; Pham, H. T.; Walter, D.; Peng, J.; Wu, Y.; Li, L.; Shen, H.; Wu, N.; Mozaffari, N.; Andersson, G.; Catchpole, K. R.; Weber, K. J.; White, T. P. Double-Sided Surface Passivation of 3D Perovskite Film for High-Efficiency Mixed-Dimensional Perovskite Solar Cells. *Adv. Funct. Mater.* **2020**, *30*, 1907962.

(13) Long, C.; Huang, K.; Chang, J.; Zuo, C.; Gao, Y.; Luo, X.; Liu, B.; Xie, H.; Chen, Z.; He, J.; Huang, H.; Gao, Y.; Ding, L.; Yang, J. Creating a Dual-Functional 2D Perovskite Layer at the Interface to Enhance the Performance of Flexible Perovskite Solar Cells. *Small* **2021**, *17*, 2102368.

(14) Zhu, H.; Ren, Y.; Pan, L.; Ouellette, O.; Eickemeyer, F. T.; Wu, Y.; Li, X.; Wang, S.; Liu, H.; Dong, X.; Zakeeruddin, S. M.; Liu, Y.; Hagfeldt, A.; Gratzel, M. Synergistic Effect of Fluorinated Passivator and Hole Transport Dopant Enables Stable Perovskite Solar Cells with an Efficiency Near 24%. *J. Am. Chem. Soc.* **2021**, *143*, 3231-3237.

(15) Liu, Z.; Qiu, L.; Ono, L. K.; He, S.; Hu, Z.; Jiang, M.; Tong, G.; Wu, Z.; Jiang, Y.; Son, D.-Y.; Dang, Y.; Kazaoui, S.; Qi, Y. A Holistic Approach to Interface Stabilization for Efficient Perovskite Solar Modules with over 2,000-Hour Operational Stability. *Nat. Energy* **2020**, *5*, 596-604.

(16) Zhang, H.; Eickemeyer, F. T.; Zhou, Z.; Mladenovic, M.; Jahanbakhshi, F.; Merten, L.; Hinderhofer, A.; Hope, M. A.; Ouellette, O.; Mishra, A.; Ahlawat, P.; Ren, D.; Su, T. S.; Krishna, A.; Wang, Z.; Dong, Z.; Guo, J.; Zakeeruddin, S. M.; Schreiber, F.; Hagfeldt, A.; Emsley, L.; Rothlisberger, U.; Milic, J. V.; Gratzel, M. Multimodal Host-Guest Complexation for Efficient and Stable Perovskite Photovoltaics. *Nat. Commun.* **2021**, *12*, 3383.

(17) Huang, Y.; Liu, T.; Li, D.; Lian, Q.; Wang, Y.; Wang, G.; Mi, G.; Zhou, Y.; Amini, A.; Xu, B.; Tang, Z.; Cheng, C.; Xing, G. Bridging the Interfacial Contact for Improved Stability and Efficiency of Inverted Perovskite Solar Cells. *Small* **2022**, *18*, 2201694.

(18) Xiong, Z.; Lan, L.; Wang, Y.; Lu, C.; Qin, S.; Chen, S.; Zhou, L.; Zhu, C.; Li, S.; Meng, L.; Sun, K.; Li, Y. Multifunctional Polymer Framework Modified SnO_2 Enabling a Photostable α-$FAPbI_3$ Perovskite Solar Cell with Efficiency Exceeding 23%. *ACS Energy Letters* **2021**, *6*, 3824-3830.

(19) Kojima, A.; Teshima, K.; Shirai, Y.; Miyasaka, T. Organometal Halide Perovskites as Visible-Light Sensitizers for Photovoltaic Cells. *J. Am. Chem. Soc.* **2009**, *131*, 6050-6051.

(20) Best research-cell efficiency chart, National Renewable Energy laboratory (NREL),. **2021**, https://www.nrel.gov/pv/assets/pdfs/best-research-cell-efficiencies-rev220630.pdf.

(21) Tian, C.; Lin, K.; Lu, J.; Feng, W.; Song, P.; Xie, L.; Wei, Z. Interfacial Bridge Using acis-Fulleropyrrolidine for Efficient Planar Perovskite Solar Cells with Enhanced Stability. *Small Methods* **2020**, *4*, 1900476.

(22) Chen, J.; Dong, H.; Zhang, L.; Li, J.; Jia, F.; Jiao, B.; Xu, J.; Hou, X.; Liu, J.; Wu, Z. Graphitic

Carbon Nitride Doped SnO_2 Enabling Efficient Perovskite Solar Cells with PCEs Exceeding 22%. *J. Mater. Chem. A* **2020**, *8*, 2644-2653.

(23) Hang, P.; Xie, J.; Kan, C.; Li, B.; Zhang, Y.; Gao, P.; Yang, D.; Yu, X. Stabilizing Fullerene for Burn-in-Free and Stable Perovskite Solar Cells under Ultraviolet Preconditioning and Light Soaking. *Adv. Mater.* **2021**, *33*, 2006910.

(24) Yang, Y.; Lu, H.; Feng, S.; Yang, L.; Dong, H.; Wang, J.; Tian, C.; Li, L.; Lu, H.; Jeong, J.; Zakeeruddin, S. M.; Liu, Y.; Grätzel, M.; Hagfeldt, A. Modulation of Perovskite Crystallization Processes towards Highly Efficient and Stable Perovskite Solar Cells with MXene Quantum Dot-Modified SnO_2. *Energy Environ. Sci.* **2021**, *14*, 3447-3454.

(25) Jiang, Q.; Zhao, Y.; Zhang, X.; Yang, X.; Chen, Y.; Chu, Z.; Ye, Q.; Li, X.; Yin, Z.; You, J. Surface Passivation of Perovskite Film for Efficient Solar Cells. *Nat. Photonics* **2019**, *13*, 460-466.

(26) Hui, W.; Yang, Y.; Xu, Q.; Gu, H.; Feng, S.; Su, Z.; Zhang, M.; Wang, J.; Li, X.; Fang, J.; Xia, F.; Xia, Y.; Chen, Y.; Gao, X.; Huang, W. Red-Carbon-Quantum-Dot-Doped SnO_2 Composite with Enhanced Electron Mobility for Efficient and Stable Perovskite Solar Cells. *Adv. Mater.* **2020**, *32*, 1906374.

(27) Altinkaya, C.; Aydin, E.; Ugur, E.; Isikgor, F. H.; Subbiah, A. S.; De Bastiani, M.; Liu, J.; Babayigit, A.; Allen, T. G.; Laquai, F.; Yildiz, A.; De Wolf, S. Tin Oxide Electron-Selective Layers for Efficient, Stable, and Scalable Perovskite Solar Cells. *Adv. Mater.* **2021**, *33*, 2005504.

(28) Jang, Y.-W.; Lee, S.; Yeom, K. M.; Jeong, K.; Choi, K.; Choi, M.; Noh, J. H. Intact 2D/3D

Halide Junction Perovskite Solar Cells via Solid-Phase in-Plane Growth. *Nat. Energy* **2021**, *6*, 63-71.

(29) Wang, P.; Chen, B.; Li, R.; Wang, S.; Ren, N.; Li, Y.; Mazumdar, S.; Shi, B.; Zhao, Y.; Zhang, X. Cobalt Chloride Hexahydrate Assisted in Reducing Energy Loss in Perovskite Solar Cells with Record Open-Circuit Voltage of 1.20 V. *ACS Energy Lett.* **2021**, *6*, 2121-2128.

(30) Jung, E. H.; Chen, B.; Bertens, K.; Vafaie, M.; Teale, S.; Proppe, A.; Hou, Y.; Zhu, T.; Zheng, C.; Sargent, E. H. Bifunctional Surface Engineering on SnO_2 Reduces Energy Loss in Perovskite Solar Cells. *ACS Energy Lett.* **2020**, *5*, 2796-2801.

(31) Dong, Y.; Shen, W.; Dong, W.; Bai, C.; Zhao, J.; Zhou, Y.; Huang, F.; Cheng, Y. B.; Zhong, J. Chlorobenzenesulfonic Potassium Salts as the Efficient Multifunctional Passivator for the Buried Interface in Regular Perovskite Solar Cells. *Adv. Energy Mater.* **2022**, *12*, 2200417.

(32) Park, S. Y.; Zhu, K. Advances in SnO_2 for Efficient and Stable n-i-p Perovskite Solar Cells. *Adv. Mater.* **2022**, *34*, 2110438.

(33) Ma, R.; Ren, Z.; Li, C.; Wang, Y.; Huang, Z.; Zhao, Y.; Yang, T.; Liang, Y.; Sun, X. W.; Choy, W. C. H. Establishing Multifunctional Interface Layer of Perovskite Ligand Modified Lead Sulfide Quantum Dots for Improving the Performance and Stability of Perovskite Solar Cells. *Small* **2020**, *16*, 2002628.

(34) Zheng, T.; Fan, L.; Zhou, H.; Zhao, Y.; Jin, B.; Peng, R. Engineering of Electron Extraction and Defect Passivation via Anion-Doped Conductive Fullerene Derivatives as Interlayers for Efficient Invert Perovskite Solar Cells. *ACS Appl. Mater. Interfaces* **2020**, *12*, 24747-24755.

(35) Sun, X.; Li, X.; Li, H.; Li, Y.; Li, S.; Zheng, Y.-Z.; Tao, X. A Facile and Broadly Applicable $CdBr_2$-Passivating Strategy for Halide Migration-Inhibiting Perovskite Films and High-Performance Solar Cells. *J. Mater. Chem. A* **2021**, *9*, 14758-14767.

(36) Ono, L. K.; Liu, S. F.; Qi, Y. Reducing Detrimental Defects for High-Performance Metal Halide Perovskite Solar Cells. *Angew. Chem. Int. Ed.* **2020**, *59*, 6676-6698.

(37) Chen, B.; Rudd, P. N.; Yang, S.; Yuan, Y.; Huang, J. Imperfections and Their Passivation in Halide Perovskite Solar Cells. *Chem. Soc. Rev.* **2019**, *48*, 3842-3867.

(38) Sherkar, T. S.; Momblona, C.; Gil-Escrig, L.; Avila, J.; Sessolo, M.; Bolink, H. J.; Koster, L. J. A. Recombination in Perovskite Solar Cells: Significance of Grain Boundaries, Interface Traps, and Defect Ions. *ACS Energy Lett.* **2017**, *2*, 1214-1222.

(39) Wu, W. Q.; Rudd, P. N.; Ni, Z.; Van Brackle, C. H.; Wei, H.; Wang, Q.; Ecker, B. R.; Gao, Y.; Huang, J. Reducing Surface Halide Deficiency for Efficient and Stable Iodide-Based Perovskite Solar Cells. *J. Am. Chem. Soc.* **2020**, *142*, 3989-3996.

(40) Zheng, X.; Chen, B.; Dai, J.; Fang, Y.; Bai, Y.; Lin, Y.; Wei, H.; Zeng, X.; Huang, J. Defect Passivation in Hybrid Perovskite Solar Cells Using Quaternary Ammonium Halide Anions and Cations. *Nat. Energy* **2017**, *2*, 17102.

(41) Zhang, W.; Pathak, S.; Sakai, N.; Stergiopoulos, T.; Nayak, P. K.; Noel, N. K.; Haghighirad, A. A.; Burlakov, V. M.; deQuilettes, D. W.; Sadhanala, A.; Li, W.; Wang, L.; Ginger, D. S.; Friend, R. H.; Snaith, H. J. Enhanced Optoelectronic Quality of Perovskite Thin Films with Hypophosphorous Acid for Planar Heterojunction Solar Cells. *Nat. Commun.* **2015**, *6*, 10030.

(42) Liu, Z.; Deng, K.; Hu, J.; Li, L. Coagulated SnO_2 Colloids for High-Performance Planar Perovskite Solar Cells with Negligible Hysteresis and Improved Stability. *Angew. Chem. Int. Ed.* **2019**, *58*, 11497-11504.

(43) Bi, H.; Zuo, X.; Liu, B.; He, D.; Bai, L.; Wang, W.; Li, X.; Xiao, Z.; Sun, K.; Song, Q.; Zang, Z.; Chen, J. Multifunctional Organic Ammonium Salt-Modified SnO_2 Nanoparticles toward Efficient and Stable Planar Perovskite Solar Cells. *J. Mater. Chem. A* **2021**, *9*, 3940-3951.

(44) Yang, D.; Yang, R.; Wang, K.; Wu, C.; Zhu, X.; Feng, J.; Ren, X.; Fang, G.; Priya, S.; Liu, S. F. High Efficiency Planar-Type Perovskite Solar Cells with Negligible Hysteresis Using EDTA-Complexed SnO_2. *Nat. Commun.* **2018**, *9*, 3239.

(45) Parida, B.; Jin, I. S.; Jung, J. W. Dual Passivation of SnO_2 by Tetramethylammonium Chloride for High-Performance $CsPbI_2Br$-Based Inorganic Perovskite Solar Cells. *Chem. Mater.* **2021**, *33*, 5850-5858.

(46) Zuo, X.; Kim, B.; Liu, B.; He, D.; Bai, L.; Wang, W.; Xu, C.; Song, Q.; Jia, C.; Zang, Z.; Lee, D.; Li, X.; Chen, J. Passivating Buried Interface via Self-Assembled Novel Sulfonium Salt toward Stable and Efficient Perovskite Solar Cells. *Chem. Eng. J.* **2022**, *431*, 133209.

(47) Chen, J.; Zhao, X.; Kim, S. G.; Park, N. G. Multifunctional Chemical Linker Imidazoleacetic Acid Hydrochloride for 21% Efficient and Stable Planar Perovskite Solar Cells. *Adv. Mater.* **2019**, *31*, 1902902.

(48) Liu, G.; Zheng, H.; Ye, J.; Xu, S.; Zhang, L.; Xu, H.; Liang, Z.; Chen, X.; Pan, X. Mixed-Phase Low-Dimensional Perovskite-Assisted Interfacial Lead Directional Management for Stable

Perovskite Solar Cells with Efficiency over 24%. *ACS Energy Lett.* **2021**, *6*, 4395-4404.

(49) Xiong, Z.; Chen, X.; Zhang, B.; Odunmbaku, G. O.; Ou, Z.; Guo, B.; Yang, K.; Kan, Z.; Lu, S.; Chen, S.; Ouedraogo, N. A. N.; Cho, Y.; Yang, C.; Chen, J.; Sun, K. Simultaneous Interfacial Modification and Crystallization Control by Biguanide Hydrochloride for Stable Perovskite Solar Cells with PCE of 24.4%. *Adv. Mater.* **2022**, *34*, 2106118.

(50) Yang, L.; Feng, J.; Liu, Z.; Duan, Y.; Zhan, S.; Yang, S.; He, K.; Li, Y.; Zhou, Y.; Yuan, N.; Ding, J.; Liu, S. F. Record-Efficiency Flexible Perovskite Solar Cells Enabled by Multifunctional Organic Ions Interface Passivation. *Adv. Mater.* **2022**, *34*, 2201681.

(51) Zhou, W.; Li, D.; Xiao, Z.; Wen, Z.; Zhang, M.; Hu, W.; Wu, X.; Wang, M.; Zhang, W. H.; Lu, Y.; Yang, S.; Yang, S. Zwitterion Coordination Induced Highly Orientational Order of $CH_3NH_3PbI_3$ Perovskite Film Delivers a High Open Circuit Voltage Exceeding 1.2 V. *Adv. Funct. Mater.* **2019**, *29*, 1901026.

(52) Yang, S.; Dai, J.; Yu, Z.; Shao, Y.; Zhou, Y.; Xiao, X.; Zeng, X. C.; Huang, J. Tailoring Passivation Molecular Structures for Extremely Small Open-Circuit Voltage Loss in Perovskite Solar Cells. *J. Am. Chem. Soc.* **2019**, *141*, 5781-5787.

(53) Liu, Z.; Cao, F.; Wang, M.; Wang, M.; Li, L. Observing Defect Passivation of the Grain Boundary with 2-Aminoterephthalic Acid for Efficient and Stable Perovskite Solar Cells. *Angew. Chem. Int. Ed.* **2020**, *59*, 4161-4167.

(54) Gaulding, E. A.; Hao, J.; Kang, H. S.; Miller, E. M.; Habisreutinger, S. N.; Zhao, Q.; Hazarika, A.; Sercel, P. C.; Luther, J. M.; Blackburn, J. L. Conductivity Tuning via Doping with Electron

Donating and Withdrawing Molecules in Perovskite $CsPbI_3$ Nanocrystal Films. *Adv. Mater.* **2019**, *31*, 1902250.

(55) Zhuang, J.; Mao, P.; Luan, Y.; Chen, N.; Cao, X.; Niu, G.; Jia, F.; Wang, F.; Cao, S.; Wang, J. Rubidium Fluoride Modified SnO_2 for Planar n-i-p Perovskite Solar Cells. *Adv. Funct. Mater.* **2021**, *31*, 2010385.

(56) Bi, H.; Liu, B.; He, D.; Bai, L.; Wang, W.; Zang, Z.; Chen, J. Interfacial Defect Passivation and Stress Release by Multifunctional KPF_6 Modification for Planar Perovskite Solar Cells with Enhanced Efficiency and Stability. *Chem. Eng. J.* **2021**, *418*, 129375.

(57) Dou, J.; Zhu, C.; Wang, H.; Han, Y.; Ma, S.; Niu, X.; Li, N.; Shi, C.; Qiu, Z.; Zhou, H.; Bai, Y.; Chen, Q. Synergistic Effects of Eu-MOF on Perovskite Solar Cells with Improved Stability. *Adv. Mater.* **2021**, *33*, 2102947.

(58) Shen, L.; Song, P.; Zheng, L.; Liu, K.; Lin, K.; Tian, W.; Luo, Y.; Tian, C.; Xie, L.; Wei, Z. Perovskite-Type Stabilizers for Efficient and Stable Formamidinium-Based Lead Iodide Perovskite Solar Cells. *J. Mater. Chem. A* **2021**, *9*, 20807-20815.

(59) Jeong, M.; Choi, I. W.; Go, E. M.; Cho, Y.; Kim, M.; Lee, B.; Jeong, S.; Jo, Y.; Choi, H. W.; Lee, J.; Bae, J. H.; Kwak, S. K.; Kim, D. S.; Yang, C. Stable perovskite solar cells with efficiency exceeding 24.8% and 0.3-V voltage loss. *Science* **2020**, *369*, 1615-1620.

(60) Wu, S.; Chen, R.; Zhang, S.; Babu, B. H.; Yue, Y.; Zhu, H.; Yang, Z.; Chen, C.; Chen, W.; Huang, Y.; Fang, S.; Liu, T.; Han, L.; Chen, W. A Chemically Inert Bismuth Interlayer Enhances Long-Term Stability of Inverted Perovskite Solar Cells. *Nat. Commun.* **2019**, *10*, 1161.

(61) Wang, Q.; Phung, N.; Di Girolamo, D.; Vivo, P.; Abate, A. Enhancement in Lifespan of Halide Perovskite Solar Cells. *Energy Environ. Sci.* **2019**, *12*, 865-886.

(62) Li, M.; Gao, H.; Yu, L.; Tang, S.; Peng, Y.; Zheng, C.; Xu, L.; Tao, Y.; Chen, R.; Huang, W. Simultaneously Enhancing Efficiency and Stability of Perovskite Solar Cells Through Crystal Cross-Linking Using Fluorophenylboronic Acid. *Small* **2021**, *17*, 2102090.

(63) Chi, W.; Banerjee, S. K. Achieving Resistance against Moisture and Oxygen for Perovskite Solar Cells with High Efficiency and Stability. *Chem. Mater.* **2021**, *33*, 4269-4303.

(64) Kresse, G.; Furthmiiller, J. Efficiency of Ab-Initio Total Energy Calculations for Metals and Semiconductors Using a Plane-Wave Basis Set. *Computational Materials Science* **1996**, *6*, 15-50.

(65) Monkhorst, H. J.; Pack, J. D. Special Points for Brillouin-Zone Integrations. *Phys. Rev. B* **1976**, *13*, 5188-5192.

(66) Weller, M. T.; Weber, O. J.; Frost, J. M.; Walsh, A. Cubic Perovskite Structure of Black Formamidinium Lead Iodide, α-$[HC(NH_2)_2]PbI_3$, at 298 K. *J. Phys. Chem. Lett.* **2015**, *6*, 3209-3212.

(67) Targhi, F. F.; Jalili, Y. S.; Kanjouri, F. $MAPbI_3$ and $FAPbI_3$ Perovskites as Solar Cells: Case Study on Structural, Electrical and Optical Properties. *Results Phys.* **2018**, *10*, 616-627.

(68) Fu, Y.; Wu, T.; Wang, J.; Zhai, J.; Shearer, M. J.; Zhao, Y.; Hamers, R. J.; Kan, E.; Deng, K.; Zhu, X. Y.; Jin, S. Stabilization of the Metastable Lead Iodide Perovskite Phase via Surface Functionalization. *Nano Lett.* **2017**, *17*, 4405-4414.

(69) Hinuma, Y.; Toyao, T.; Kamachi, T.; Maeno, Z.; Takakusagi, S.; Furukawa, S.; Takigawa, I.;

Shimizu, K.-i. Density Functional Theory Calculations of Oxygen Vacancy Formation and Subsequent Molecular Adsorption on Oxide Surfaces. *J. Phys. Chem. C* **2018**, *122*, 29435-29444.

(70) Ding, Y.; Shen, Y.; Peng, C.; Huang, M.; Hu, P. Unraveling the Photogenerated Electron Localization on the Defect-Free $CH_3NH_3PbI_3$(001) Surfaces: Understanding and Implications from a First-Principles Study. *J. Phys. Chem. Lett.* **2020**, *11*, 8041-8047.

Table of Contents